

Taking into Account the Ion-Induced Dipole Interaction in the Nonbonded Model of Ions

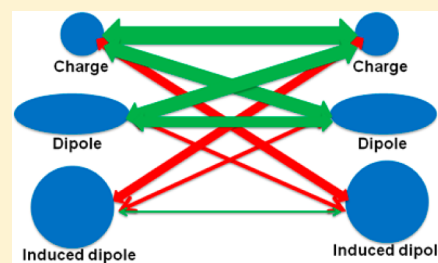
Pengfei Li and Kenneth M. Merz, Jr.*

Department of Chemistry Quantum Theory Project, 2328 New Physics Building, University of Florida, Gainesville, Florida 32611-8435, United States

Department of Chemistry, Department of Biochemistry and Molecular Biology, Michigan State University, 578 S. Shaw Lane, East Lansing, Michigan 48824-1322, United States

Supporting Information

ABSTRACT: Metal ions exist in almost half of the proteins in the protein databank, and they serve as structural, electron-transfer, and catalytic elements in the metabolic processes of organisms. Molecular dynamics (MD) simulation is a powerful tool that provides information about biomolecular systems at the atomic level. Coupled with the growth in computing power, algorithms like the particle mesh Ewald (PME) method have become the accepted standard when dealing with long-range interactions in MD simulations. The nonbonded model of metal ions consists of an electrostatic plus 12–6 Lennard-Jones (LJ) potential and is used largely because of its speed relative to more accurate models. In previous work we found that ideal parameters do not exist that reproduce several experimental properties for M(II) ions simultaneously using the nonbonded model coupled with the PME method due to the underestimation of metal ion-ligand interactions. Via a consideration of the nature of the nonbonded model, we proposed that the observed error largely arises from overlooking charge-induced dipole interactions. The electrostatic plus 12–6 LJ potential model works reasonably well for neutral systems but does struggle with more highly charged systems. In the present work we designed and parametrized a new nonbonded model for metal ions by adding a $1/r^4$ term to the 12–6 model. We call it the 12–6–4 LJ-type nonbonded model due to its mathematical construction. Parameters were determined for 16 +2 metal ions for the TIP3P, SPC/E, and TIP4P_{EW} water models. The final parameters reproduce the experimental hydration free energies (HFE), ion-oxygen distances (IOD) in the first solvation shell, and coordination numbers (CN) accurately for most of the metal ions investigated. Preliminary tests on MgCl_2 at different concentrations in aqueous solution and Mg^{2+} –nucleic acid systems show reasonable results suggesting that the present parameters can work in mixed systems. The 12–6–4 LJ-type nonbonded model is readily adopted into standard force fields like AMBER, CHARMM, and OPLS-AA with only a modest computational overhead. The new nonbonded model does not consider charge-transfer effects explicitly and, hence, may not be suitable for the simulation of systems where charge-transfer effects play a decisive role.



INTRODUCTION

Nearly 50% of all proteins contain metal ions.^{1–4} Even if most of them are present in trace quantities, they are indispensable and play significant biological roles. They interact with amino acids, nucleic acids, lipids, and carbohydrates, playing a role in a wide range of biological functions including structural, electron transfer, and catalysis.^{1–14}

Molecular dynamics (MD) simulation is a powerful theoretical tool used to investigate chemical and biological systems. It provides detailed, dynamic information at the atomic level. The particle mesh Ewald (PME) method is now the de facto standard method used to calculate the long-range electrostatic energy in periodic boundary simulation cells.^{15–18} It calculates the short-range interactions in real space while the long-range interactions are developed in Fourier space. Importantly, it decreases the time complexity of MD simulations from $O(N^2)$ to $O(N \log N)$ with reliable precision.^{15–18}

A number of potential functions have been designed for metal-ion-containing systems.^{19–33} For example, Gresh et al. developed the Sum of Interactions Between Fragments computed ab initio (SIBFA) method¹⁹ and studied several Zn-containing proteins.^{20–23} This method gave accurate results comparable to the high-level ab initio calculations on which the method is based. However, the relatively complex parametrization process limits its application in MD simulations of metalloproteins. Stote and Karplus parametrized the nonbonded model for the zinc ion.²⁴ It uses a potential function with an electrostatic term plus a 12–6 Lennard-Jones (LJ) potential and has been widely used due to its simplicity of form and high simulation efficiency. It can simulate ligand exchange processes, but in previous research we found that no ideal parameter set exists that can reproduce different kinds of experimental properties simultaneously for a broad range of

Received: August 24, 2013

Published: October 29, 2013

ions. In particular, the nonbonded model underestimates the interaction between the metal ions and the surrounding water molecules and traditionally has neglected polarizability.³⁴ Pang developed the cationic dummy atom approach and showed it could reproduce the experimental structures of two zinc complexes in phosphotriesterase (PTE) during the MD simulation.²⁵ Chillemi and D'Angelo proposed a model with an effective two-body potential to model Zn^{2+} , Ni^{2+} , and Co^{2+} ions in water.²⁶ Reasonable results were obtained, but the functional form hinders its straightforward implementation in MD simulations of protein systems due to the many parameters that need to be determined as the number of atom types increase. Sakharov and Lim designed the Charge-Transfer Polarization (CTPOL) Potential Energy Function (PEF) and simulated several Zn^{2+} , Cd^{2+} , and Hg^{2+} containing proteins.^{27,28} A linear charge transfer model was employed in this potential and the experimentally observed structures were reproduced during the MD simulations.

Peters et al. designed the Metal Center Parameter Builder (MCPB) software to accelerate the parametrization of metal centers with the bonded model in the AMBER force field.²⁹ It treats the interaction of the metal ions with the surrounding residues by a summation of bond, angle, torsion, electrostatic, and VDW terms. However, the bonded model cannot model coordination number changes and ligand switching processes due to its functional form. Wu et al. proposed a Short-Long-Effective-Function (SLEF) for Zn-containing proteins.³¹ The parameters were optimized from quantum mechanics/molecular mechanics (QM/MM) MD simulations, and the simulation results were consistent with several experimentally determined protein structures with different coordination modes. Wu et al. parametrized and simulated the Zn–water system using the Atomic Multipole Optimized Energetic for Biomolecular Applications (AMOEBA) force field.³⁰ They found that the charge-transfer energy diminishes when zinc is transferred from the gas phase to the aqueous phase and could be incorporated into the polarization energy to some extent. Zhang et al. performed simulations with several Zn-containing proteins also based on the AMOEBA force field.³² They found that the polarization effect plays an important role in defining the geometry and coordination of the proteins they investigated. Furthermore, they found that it was difficult to model the polarization effect with a fixed-charge model implicitly due to its ligand-dependent characteristics. Zhu et al. designed and parametrized the Quantum Calibrated Polarizable Charge-Transfer (QPCT) force field for several Zn containing proteins.³³ It reproduced the potential energy surface (PES) between the metal ion and its ligands accurately but could not simulate the ion insertion or extraction process.

Herein, we have developed a new nonbonded model for metal ions. The 12–6 plus electrostatics nonbonded model explicitly includes the Pauli repulsion and induced dipole–induced dipole interactions via the Lennard-Jones potential, while the charge–charge, charge–dipole, and dipole–dipole interactions and represented by the Coulomb potential. However, it does not take into account the charge-induced dipole interaction and the dipole–induced dipole interaction explicitly. The former interaction is the dominant one of these two types of interactions in the case of metal ions and its inclusion, in principle, would greatly improve a nonbonded model representing ions. The standard nonbonded model is reasonable for neutral systems, while for highly charged

systems, the charge-induced dipole interaction becomes very significant and needs to be considered.

With these considerations, we decided to add an r^{-4} term into the standard 12–6 LJ nonbonded model in order to include the ion-induced dipole interaction. Unlike the 12–6 LJ nonbonded model, the new 12–6–4 LJ-type model does reproduce different experimental values at the same time after selecting appropriate parameters. The final parameters reproduced the experimental HFE values by ± 1 kcal/mol, the IOD and CN values accurately for almost all of the M(II) ions investigated. Meanwhile, the final parameters were consistent with the analytical formulation of the charge-induced dipole potential. Furthermore, the new nonbonded model is compatible with force field like AMBER,³⁵ CHARMM,³⁶ and OPLS-AA³⁷ with almost no additional computing cost. Even so, attention should be paid when the new nonbonded model is employed in systems with strong charge-transfer effects since it may be unphysical to treat the central metal atom as an actual “ion” in such cases.

METHODS

Potential Function Form. The form of the nonbonded model in the AMBER force field (FF) is as follows:

$$U_{ij}(r_{ij}) = \varepsilon_{ij} \left[\left(\frac{R_{\min,ij}}{r_{ij}} \right)^{12} - 2 \left(\frac{R_{\min,ij}}{r_{ij}} \right)^6 \right] + \frac{e^2 Q_i Q_j}{r_{ij}} \\ = \frac{C_{12}^{ij}}{r_{ij}^{12}} - \frac{C_6^{ij}}{r_{ij}^6} + \frac{e^2 Q_i Q_j}{r_{ij}} \quad (1)$$

Where, e is the proton charge while Q_i and Q_j are the partial charge of two particles and r_{ij} is the distance between the two particles. $R_{\min,ij}$ is the distance at which two particles have a minimum in the LJ potential while ε_{ij} is the well depth. The ε_{ij} and $R_{\min,ij}$ terms follow the Lorentz–Berthelot combining rule:

$$R_{\min,ij} = \frac{R_{\min,ii} + R_{\min,jj}}{2} = R_{\min,i} + R_{\min,j} \quad (2)$$

$$\varepsilon_{ij} = \sqrt{(\varepsilon_i \varepsilon_j)} \quad (3)$$

Our modified nonbonded potential for the interaction between a metal ion and its surroundings is the following:

$$U_{ij}(r_{ij}) = \frac{C_{12}^{ij}}{r_{ij}^{12}} - \frac{C_6^{ij}}{r_{ij}^6} - \kappa \frac{C_6^{ij}}{r_{ij}^4} + \frac{e^2 Q_i Q_j}{r_{ij}} \\ = \varepsilon_{ij} \left[\left(\frac{R_{\min,ij}}{r_{ij}} \right)^{12} - 2 \left(\frac{R_{\min,ij}}{r_{ij}} \right)^6 - 2\kappa R_{\min,ij}^2 \left(\frac{R_{\min,ij}}{r_{ij}} \right)^4 \right] \\ + \frac{e^2 Q_i Q_j}{r_{ij}} \quad (4)$$

The potential function representing the interactions between water molecules have not been modified because they have already been parametrized to reproduce relevant experimental quantities. Here we used a κC_6^{ij} (here κ has the unit \AA^{-2}) to represent the C_4^{ij} term rather than designing a new set C_4^{ij} parameters for the metal ion and oxygen atoms of the water molecules. Since different water models have different parameters, we have to create unique M(II) parameter sets for each water model. The present work developed parameters

for three widely used water models: TIP3P,³⁸ SPC/E,³⁹ and TIP4P_{EW}.⁴⁰

Thermodynamic Integration. Thermodynamic integration is a powerful tool to study the free energy changes of two states of a system.^{41–48} It employs a mixing Hamiltonian between the initial and final state:

$$V(\lambda) = (1 - \lambda)^k V_0 + [1 - (1 - \lambda)^k] V_1 \quad (5)$$

The potential function of the initial state is represented by V_0 while the final state is expressed as V_1 , λ is a real number between 0 and 1 which indicates the mixing extent between the two states. k is an integer, and when $k = 1$, we are using linear mixing. For the hydration free energy determination of M(II) ions we employed a two-step TI method: a VDW scaling step followed by an electrostatic plus polarization energy (r^{-4} term) scaling step. For the VDW scaling part, a linear soft-core scaling method⁴⁸ was employed, which has the functional form:

$$V_{\text{soft-core VDW}} = 4\epsilon(1 - \lambda) \left[\frac{1}{\left[\alpha\lambda + \left(\frac{r_{ij}}{\sigma}\right)^6 \right]^2} - \frac{1}{\alpha\lambda + \left(\frac{r_{ij}}{\sigma}\right)^6} \right] \quad (6)$$

In which, the r_{ij} is the distance between the vanishing particle with the other particles. The term α is a constant which is set to 0.5, and σ is the distance at which the potential between the two particles is zero, which is equal to $R_{\text{min},ij}/2^{1/6}$. This functional form solves the “end-point catastrophe” problem in an efficient way. While for the charge and polarization scaling step, we employed the linear scaling algorithm (with $k = 1$ in eq 5).

As shown in eq 7, the derivative of $\partial V/\partial \lambda$ obtained from the simulation can be integrated to yield the free energy of the entire hydration process. With Gaussian quadrature, the final free energy is obtained as given in eq 8.

$$\Delta G = G(\lambda = 1) - G(\lambda = 0) = \int_0^1 \langle \partial V/\partial \lambda \rangle_\lambda d\lambda \quad (7)$$

$$\Delta G = \sum w_i \langle \partial V/\partial \lambda \rangle_i \quad (8)$$

For the VDW step, we employed a three-window scaling process with the λ values set to 0.1127, 0.5, and 0.88729. While for the charge and polarization step, nine-window scaling was used with λ values of 0, 0.2544, 0.12923, 0.29707, 0.5, 0.70292, 0.87076, 0.97455, and 1. The simulation of each window used the last snapshot of the former window as its starting structure, and the weights of the windows with $\lambda = 0$ or 1 is set to zero in eq 8 which only serve to equilibrate the system and were not included in the final calculation of the hydration free energy.

Simulation Procedures. *a. Calculation of the HFE Values.* A dummy atom was solvated in a $\sim(32 \text{ \AA} \times 32 \text{ \AA} \times 32 \text{ \AA})$ cubic water box with the closest water molecule being 1.5 Å away from the dummy atom. There were a total of 722 water molecules for the TIP3P and SPC/E water boxes while for the TIP4P_{EW} water box the number was 732. Minimizations were performed using 1000 steps of steepest descent followed by 1000 steps of conjugate gradient. Next a 500 ps heating step was performed using the NVT ensemble to increase the temperature from 0 to 300 K. Afterward a 500 ps MD simulation was performed using the NPT ensemble at 300 K and 1 atm to equilibrate the system. The final snapshot of the NPT equilibration was used as the initial structure in the VDW scaling step.

The HFE calculation was performed using the thermodynamic cycle shown in Figure 1, in which ΔG_{VDW} , $\Delta G_{\text{Ele+Pol}}$

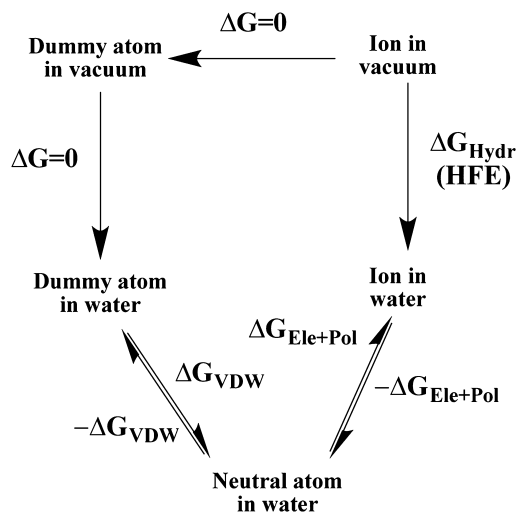


Figure 1. Thermodynamic cycle for HFE calculations.

$-\Delta G_{\text{Ele+Pol}}$ and $-\Delta G_{\text{VDW}}$ values were obtained successively, and the final HFE value was obtained by averaging $(\Delta G_{\text{VDW}} + \Delta G_{\text{Ele+Pol}})$ and $(-\Delta G_{\text{Ele+Pol}} - \Delta G_{\text{VDW}})$. In the VDW scaling step, each window used 100 ps of equilibration and 200 ps of sampling, while for the charge and polarization scaling step, each window used 50 ps of equilibration and 150 ps of sampling. All the TI scaling procedures were performed using the NPT ensemble at 300 K and 1 atm. Isotropic position scaling was used with a pressure relaxation time equal to 10 ps.

Finally, two different methods were employed to evaluate the computational uncertainty of the simulated HFE values. These analyses are presented in excel spreadsheets provided in the Supporting Information (SI) as uncertainty analysis set 1 and 2, where Table 3 in the spreadsheets correspond to Table 3 in the text. Moreover, in the SI we have associated error analyses for the scanning studies carried out herein (see below). The uncertainty of ΔG_{VDW} and $\Delta G_{\text{Ele+Pol}}$ were treated separately and finally summed as the uncertainty of the HFE values. Set 1 calculated the uncertainty of the ΔG_{VDW} term by splitting the forward 200 ps and backward 200 ps into two 100 ps segments and calculated the ΔG_{VDW} for each segment independently. The final uncertainty was obtained from the standard deviation of these four values. The uncertainty of $\Delta G_{\text{Ele+Pol}}$ was obtained in a similar manner by dividing the forward 150 ps and backward 150 ps into four 75 ps segments for the uncertainty analysis. Set 2 used eq 9 to perform the uncertainty estimation. Here the τ_A and $(A_c^2)^{1/2}$ are the autocorrelation time and standard deviation of the observable A , respectively. T is the sampling time while δA is the standard deviation σ of the final value of observable A . All of the final results were represented as $A \pm \sigma$. We used $\tau_A = 500$ ps for the VDW scaling part while $\tau_A = 250$ ps for the electrostatic plus polarization scaling step. These values were determined from several test simulations and are consistent with the research of Shirts et al.⁴⁹

$$\delta A = \sqrt{\langle A^2 \rangle_c} \times \sqrt{2\tau_A/T} \quad (9)$$

The set 1 analysis yielded computed uncertainties in the range of 0.1–1.7 kcal/mol (with an average of ~ 0.7 kcal/mol and a standard deviation ~ 0.3 kcal/mol) for the computed

HFEs. While the set 2 analysis yielded uncertainties in the range of 0.9–1.0 kcal/mol (with the average and standard deviation being ~ 0.9 and ~ 0.1 kcal/mol, respectively). Overall, we conservatively estimate that there is ~ 1 kcal/mol uncertainty for the computed HFE values using the parameters derived herein.

b. Calculation of the Structural Properties. A metal ion with +2 charge was solvated in the center of a $\sim (32 \text{ \AA} \times 32 \text{ \AA} \times 32 \text{ \AA})$ water box (for TIP4P_{EW} water model a $\sim (36 \text{ \AA} \times 36 \text{ \AA} \times 36 \text{ \AA})$ cubic water box with 1085 water molecules was used). Minimization was performed using 1000 steps of steepest descent minimization followed by 1000 steps of conjugate gradient. Afterward 500 ps of NVT simulation was performed to heat the system from 0 to 300 K. Then a 500 ps NPT equilibration simulation was run followed by 2 ns of sampling at 300 K and 1 atm. The trajectory snapshots were stored every 0.5 ps for further analysis. The radial distribution function (RDF) was obtained from the trajectory with a resolution of 0.01 Å in which the density was based on the average volume of the entire trajectory. The IOD values were obtained by using a two-part quadratic fitting procedure of the RDF. The first quadratic fitting was done using points within ± 0.1 Å of the peak (in total 21 points, at a 0.01 Å interval), the second quadratic fitting was performed using data within ± 0.1 Å of the point which is closest to the apex value of the first fitting (again a total of 21 points was used). The IOD value was finally determined from the peak value of the second quadratic fitting. The CN values were obtained by integrating the RDF from the origin to the first minimum.

For all MD simulations performed in present work, periodic boundary conditions (PBC) were utilized, while PME was employed to calculate the long-range interactions and forces. The time-step was set to 1 fs and the cut off was set to 10 Å. Langevin temperature control was used with a collision frequency of 5.0 ps^{-1} , SHAKE^{50,51} was used on the water molecules during the simulations.

RESULTS AND DISCUSSION

In this work we designed parameters based on three different experimental values: HFE, IOD, and the CN values of the first solvation shell. HFE values represent the thermodynamic properties while the other two represent structural properties. In our previous research, we found that it is impossible to reproduce all three experimental quantities at the same time in simulations using the “standard” nonbonded model with parameters spanning the typical LJ space.³⁴ This is because the nonbonded model underestimates the interaction energy between the ion and surrounding water molecules and this underestimation, as expected, decreases with the increasing size of the metal ion’s radius.

Force fields are designed to accurately describe the interactions in a complex system using relatively easy to compute functional forms and consist of terms representing bonded interactions (bond, angle, and dihedral terms) and nonbonded interactions. The nonbonded model in typical force fields is composed of an electrostatic and VDW term. Point charges are obtained in a number of ways, but in the AMBER force field restrained electrostatic potential (RESP) charges⁵² are used and they approximate charge–charge, charge–dipole, and dipole–dipole interactions. The 12–6 Lennard-Jones potential is used to represent the VDW interaction, which consists of Pauli repulsion and induced dipole–induced dipole (so-called dispersion) interactions. However, as shown in

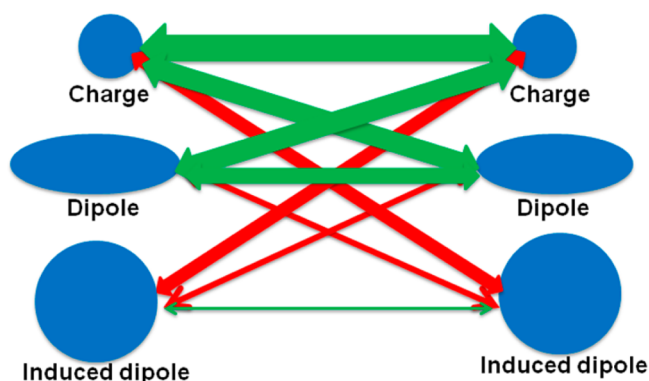


Figure 2. Scheme representing intermolecular interactions: the green double-headed arrow and red double-headed arrow represent the interactions, which included and not included in the 12–6 nonbonded model, respectively.

Figure 2, generally there is no term representing the charge–induced dipole and dipole–induced dipole interaction explicitly in the nonbonded model. Furthermore, among these two interactions, the charge–induced dipole interaction is the dominant one in the case of M(II) ions and it has a potential functional form proportional to r^{-4} . In light of this, we added a new term into the nonbonded model between the charged ion and the surrounding particles to represent the charge–induced dipole interaction. The new potential was given in eq 4, and the parameters that need to be determined are $R_{\min}/2$, ϵ , and κ . We determined the final parameters for various +2 metal ions using different water models by utilizing the experimental HFE, IOD, and CN values shown in Table 1. Details of the process used to design our parameter sets is described in the following paragraphs.

First, we scanned the parameter space where $R_{\min}/2$ and κ represented the two axes. The range investigated for $R_{\min}/2$ was between 0.8 and 2.3 Å at 0.1 Å intervals, while κ ranged between 0 and 6 \AA^{-2} with an interval of 1 \AA^{-2} . The ϵ value was fixed for each $R_{\min}/2$ value in the present work by using the NGC fitted in our earlier study³⁴ where the $R_{\min}/2$ and ϵ values had a relationship of $-\log(\epsilon) = C_1 e^{C_2(R_{\min}/2)}$ with $C_1 = 57.36$ and $C_2 = -2.471$. To be consistent with our former work, the final parameters represent $R_{\min}/2$ with three decimal places, ϵ with eight and κ with three.

The HFE, IOD, and CN values from our parameter space scan for the TIP3P, SPC/E, and TIP4P_{EW} water models are given in Supporting Information (SI) Tables SI.1 and SI.2. The HFE and IOD fitting curves were obtained based on these data. The curve fitting procedure is also provided in the SI. It is similar to the method used previously with the only difference being for the IOD fitting curve. The intention of this modification was to obtain enough meaningful points to fit the IOD curves.

Using the TIP3P water model as an example, we present the HFE and IOD fitting curves we obtained in Figure 3. In contrast to our earlier work, in which the HFE and IOD fitting curve for each metal ion were nearly parallel with each other,³⁴ the HFE and IOD fitting curves for each metal ion in the present work have an intersection point. The fitting curves for the Be^{2+} ion is not shown in Figure 3 because the intersection point of its HFE and IOD fitting curves is beyond the scanning range examined for the other ions. Because of the presence of an intersection point, there exists a set of parameters which

Table 1. Experimental Values of the HFE, IOD, and CN of the First Solvation Shell for M(II) Metal Ions

ions	HFE (kcal/mol) ^a	relative HFE (M ²⁺ –Cd ²⁺) (kcal/mol)	CN	IOD (Å)
Be ²⁺	–572.4	–152.9	4 ^b	1.67 ^b
Cu ²⁺	–480.4	–60.9	6 ^b	Eq: 1.96 ± 0.04 Ax: 2.40 ± 0.10 ^b weighted mean distance: 2.11 ^f
Ni ²⁺	–473.2	–53.7	6 ^b	2.06 ± 0.01 ^b
Zn ²⁺	–467.3	–47.8	6 ^b	2.09 ± 0.06 ^b
Co ²⁺	–457.7	–38.2	6 ^b	2.10 ± 0.02 ^b
Cr ²⁺	–442.2	–22.7	6 ^d	Eq: 2.08 ^d
Fe ²⁺	–439.8	–20.3	6 ^b	2.11 ± 0.01 ^b
Mg ²⁺	–437.4	–17.9	6 ^b	2.09 ± 0.04 ^b
V ²⁺	–436.2	–16.7	6 ^c	2.21 ^c
Mn ²⁺	–420.7	–1.2	6 ^b	2.19 ± 0.01 ^b
Hg ²⁺	–420.7	–1.2	6 ^b	2.41 ^b
Cd ²⁺	–419.5	0.0	6 ^b	2.30 ± 0.02 ^b
Ca ²⁺	–359.7	59.8	8 ^e	2.46 ^e
Sn ²⁺	–356.1	63.4	6 ^d	Eq: 2.33–2.34 ^d Ax: 2.38–2.90 ^d weighted mean distance: 2.62 ^b
Sr ²⁺	–329.8	89.7	8–15 ^d	2.64 ± 0.04 ^b
Ba ²⁺	–298.8	120.7	9 ^g	2.83 ^g

^aAll the experimental hydration free energies were obtained from Marcus.⁵³ ^bFrom Marcus.⁵⁴ ^cFrom Miyana et al.⁵⁵ ^dFrom Ohtaki and Radnai.⁵⁶ ^eFrom Jalilehvand, Spångberg, et al.⁵⁷ ^fCalculated by the authors from the experimental data. ^gFrom Smirnov and Trostin.⁵⁸

both reproduce the experimental HFE and IOD values simultaneously.

After obtaining the intersection point between the two fitting curves and fine-tuning the resultant parameters, we obtained the final parameters for each metal ion. These parameters are shown in Table 2, and the simulated HFE, IOD, and CN values are given in Table 3. While the corresponding C_4 parameters are shown in Table 4. Herein, our final parameters reproduce the HFE to within ± 1 kcal/mol of experiment and simultaneously reproduce most of the IOD and CN values with good accuracy.

$$U_{q-\alpha_0} \approx -\frac{1}{2}\alpha_0\left(\frac{q}{4\pi\epsilon_0\epsilon_r r^2}\right)^2 \cos \theta \quad (10)$$

$$C_4 \approx -\frac{1}{2}\alpha_0\left(\frac{q}{4\pi\epsilon_0\epsilon_r}\right)^2 \cos \theta \quad (11)$$

To further assess our final parameters, we employed eq 11, which is based on the equation for the charge–induced dipole interaction (eq 10), to approximate the C_4 term between the M(II) ion and the surrounding water molecules. In these two equations, q is the charge of the metal ion and α_0 is the induced dipole of the particles interacting with the metal ion. θ is the angle between the induced dipole and electronic field created by the metal ion. To calculate the C_4 term between an M(II) ion and a water molecule, we assumed $\alpha_0 = 1.444 \text{ Å}^3$ (obtained from the book of Eisenberg and Kauzmann⁵⁹), $q = +2e$, $\theta = 0^\circ$, and $\epsilon_r = 1$ (as in the AMBER FF³⁵). This analysis yields a value for C_4 of $\sim 960.0 \text{ Å}^4 \cdot \text{kcal/mol}$, which is the same order magnitude but bigger than our final parameters. This may arise because the fixed-charge water models are overpolarized in their original design. For example, the TIP3P and SPC/E water molecules all have a dipole of 2.35 D while the TIP4P_{EW} water molecule has a dipole of 2.32 D. These values are greater than the experimentally determined permanent dipole (1.855 D)⁶⁰ for the gas-phase water molecule. The fixed-charge water model included the polarization effect in to some extent by over fitting the permanent dipole moment while omitting the induced dipole. This approximation may also give some insight into to the nonbonded model's tendency to underestimate solvation

free energies for +2 metal ions. In particular, the three water models investigated in the present work all have a smaller dipole moments than the total dipole for a liquid phase water molecule determined from experiment ($2.95 \pm 0.2 \text{ D}$)⁶¹ and ab initio MD simulation ($\sim 3.0 \text{ D}$).⁶² In the work of Wu et al., they found that the charge transfer effect of solvated Zn²⁺ ion could be incorporated into the polarization energy of the AMOEBA water molecules when representing the charge and the polarizability of Zn²⁺ as $+2e$ and 0.260 Å^3 , respectively.³⁰ Which may come from the fact that the AMOEBA water model has a total dipole of 2.54 D,⁶³ which is bigger than that of the three nonpolarizable water models investigated here.

Meanwhile, as shown in Table 4, the C_4 term generally decreases when the metal ion's radius increases. This may arise from the $\cos \theta$ term in eq 11 because nearby water molecules would be more readily polarized than more remote ones. When there is a greater distance between the metal ion and its surrounding water molecules, the latter would be more randomly oriented due to a reduction in the influence arising from interactions with the metal ion. Table 4 also shows that the TIP3P and SPC/E water models give very similar C_4 values while TIP4P_{EW} gives slightly larger values. This may arise from the fact that the negative charge of the TIP4P_{EW} water model is on the dummy atom, which is placed on the bisector of the hydrogen–oxygen–hydrogen angle, yielding a slightly smaller dipole, which is then responsible for the observed underestimation of the ion–water interaction. This representation results in a greater distance between the negative charge on water and the positive charge on the metal ion than present on the three-site water model and, thereby, increases the C_4 value.

For the alkaline earth metal ions, the C_4 term decreases monotonically with an increase of the metal ion's radius. As discussed above, this may due to the shielding of the metal ion's ability to polarize the surrounding water molecules when the ion's radius increases. Another interesting observation is that although Be²⁺ is the smallest ion studied in the present work, it does not have the largest C_4 value among all the metal ions. It is C_4 value is around $190 \text{ Å}^4 \cdot \text{kcal/mol}$, $\sim 20\%$ less than the value obtained for Zn²⁺. This may arise from a significant charge-transfer effect between Be²⁺ and its surrounding water molecules. Pavlov et al. showed that there is about 1.28e

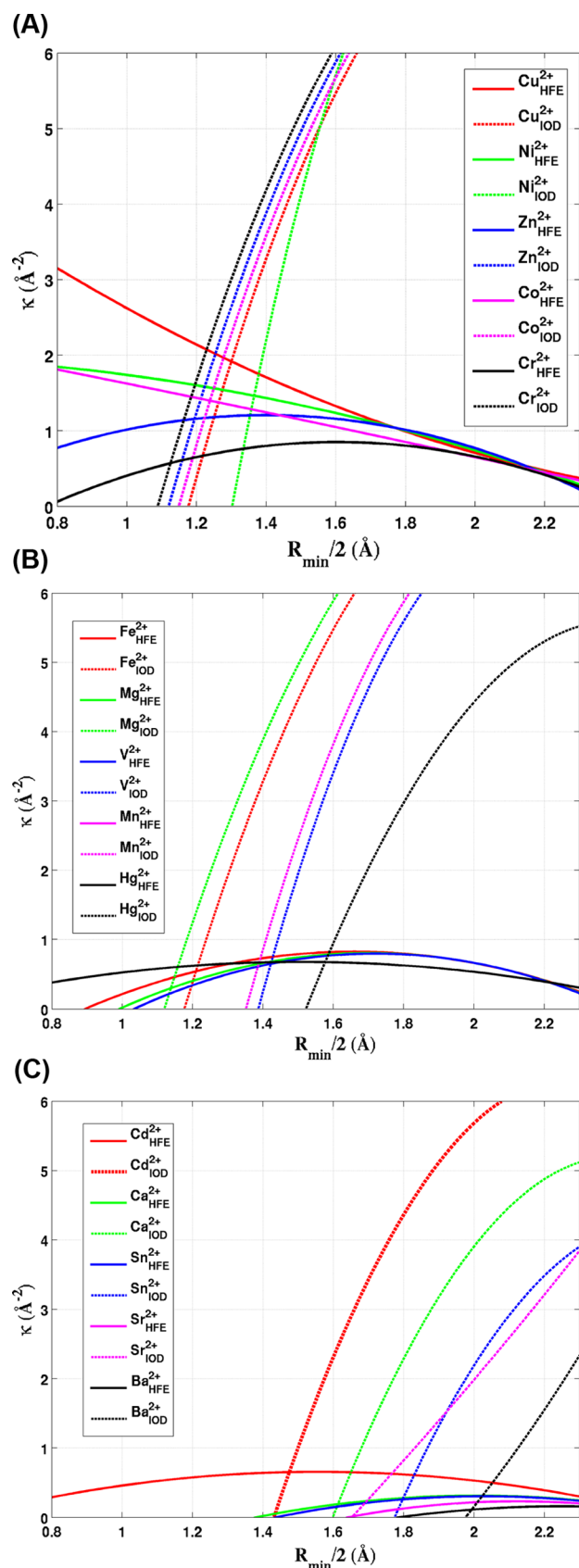


Figure 3. (a) HFE and IOD fitting curves for the Cu^{2+} , Ni^{2+} , Zn^{2+} , Co^{2+} , and Cr^{2+} ions in TIP3P water. (b) HFE and IOD fitting curves for the Fe^{2+} , Mg^{2+} , V^{2+} , Mn^{2+} , and Hg^{2+} ions in TIP3P water. (c) HFE and IOD fitting curves for the Cd^{2+} , Ca^{2+} , Sn^{2+} , Sr^{2+} , and Ba^{2+} ions in TIP3P water.

transferred from the surrounding water molecules to the Be^{2+} ion in the $[\text{Be}(\text{H}_2\text{O})_4]^{2+}$ complex according to a Mulliken population analysis at the B3LYP/6-311+G(2d,2p) level of theory.⁶⁴

For the metal ions in the first transition row, the C_4 term is also consistent with the Irving–William series⁶⁵ where the magnitude of C_4 varies as $\text{Mn}^{2+} < \text{Fe}^{2+} < \text{Co}^{2+} < \text{Ni}^{2+} < \text{Cu}^{2+} > \text{Zn}^{2+}$, which arises due to the interplay between covalent and ionic interactions.⁶⁶ Through density functional theory, it was found that the charge transfer effect follows the Irving–William series sequence.⁶⁶ There is also a larger bond order between the Cu^{2+} ion and it is ligating ligands than for the other M(II) ions in the Irving–William series. Moreover, the ionic and covalent interactions can compensate one another. When there is a stronger charge transfer, there is usually a stronger covalent interaction but a weaker ionic interaction between the metal ion and its ligands.⁶⁶ Another thing to bear in mind is that the d^9 electronic structure of the $\text{Cu}(\text{H}_2\text{O})_6^{2+}$ complex results in a Jahn–Teller effect where the axial bond lengths are about 0.44 Å longer than the equatorial ones.⁵⁴ This effect could not be modeled using the present nonbonded potential function due to the isotropic approximation employed.

Cd^{2+} has a smaller C_4 value than Zn^{2+} , due to the longer distance between the Cd^{2+} ion and the surrounding water molecules. However, it is interesting that Hg^{2+} , the ion that has the highest atomic number among these +2 metal ions, has a C_4 value bigger than Zn^{2+} . Tai and Lim also found that Hg^{2+} is a much better charge acceptor than Zn^{2+} according to their calculations,⁶⁷ which they ascribed this to relativistic effects. Hg^{2+} can accept more negative charge from its surrounding ligands than the Zn^{2+} ion. This phenomenon not only happened with “soft” sulfur ligand atoms but also with ligands containing “harder” atoms like nitrogen and oxygen.⁶⁷

The Sn^{2+} cation also has an unusual C_4 value among these +2 metal ions. This may be because of its two outermost electrons occupy a 5p orbital and Sn also has a +4 oxidation state that is slightly more stable. Experiments have also revealed two different bond lengths with an asymmetric structure in the first hydration shell which might not be well reproduced with our model.⁵⁶

To further test the 12–6–4 nonbonded model proposed here, we performed simulations on aqueous MgCl_2 at different concentrations and on a Mg^{2+} -nucleic acid system with different parameter sets. In total three sets of parameters were tested in these simulations. These included the original AMBER FF parameter for Mg^{2+} , the 12–6 LJ compromise (CM) parameter set for Mg^{2+} ,³⁴ and the 12–6–4 parameters developed in the present work. During the simulations, the C_4 parameter in the 12–6–4 model between the metal ion and each atom type are roughly evaluated by the following equation:

$$C_4(\text{atom type}) = \frac{C_4(\text{H}_2\text{O})}{\alpha_0(\text{H}_2\text{O})} \times \alpha_0(\text{atom type}) \quad (12)$$

The $C_4(\text{H}_2\text{O})$ term was taken from Table 4. And the polarizabilities of each atom type used in the simulations are given in Supporting Information Table SI.3. The simulation conditions for these tests are discussed in the SI. For the MgCl_2 systems, a TIP3P water box (~2000 waters) was used and three different concentration levels (0.25, 0.5, and 1.0 M) were modeled. For the nucleic acid system, the pdb structure of the DNA fragment (PDB ID: 1D23) and TIP4P_{EW} waters were

Table 2. Final Optimized Parameters for the Three Water Models

	TIP3P			SPC/E			TIP4P _{EW}		
	$R_{\min}/2$ (Å)	ϵ (kcal/mol)	κ (Å ⁻²)	$R_{\min}/2$ (Å)	ϵ (kcal/mol)	κ (Å ⁻²)	$R_{\min}/2$ (Å)	ϵ (kcal/mol)	κ (Å ⁻²)
Be ²⁺	1.203	0.00116124	10.200	1.205	0.00120058	9.800	1.205	0.00120058	11.650
Cu ²⁺	1.476	0.03198620	1.789	1.482	0.03364841	1.758	1.475	0.03171494	2.000
Ni ²⁺	1.431	0.02133669	1.742	1.424	0.01995146	1.714	1.430	0.02113456	2.035
Zn ²⁺	1.455	0.02662782	1.623	1.454	0.02639002	1.588	1.450	0.02545423	1.877
Co ²⁺	1.458	0.02735051	1.442	1.457	0.02710805	1.410	1.455	0.02662782	1.688
Cr ²⁺	1.431	0.02133669	1.120	1.424	0.01995146	1.096	1.425	0.02014513	1.440
Fe ²⁺	1.457	0.02710805	1.128	1.450	0.02545423	1.095	1.450	0.02545423	1.386
Mg ²⁺	1.437	0.02257962	1.046	1.429	0.02093385	0.987	1.436	0.02236885	1.362
V ²⁺	1.494	0.03715368	1.080	1.502	0.03962711	1.060	1.495	0.03745682	1.280
Mn ²⁺	1.485	0.03450196	0.851	1.495	0.03745682	0.828	1.485	0.03450196	1.067
Hg ²⁺	1.641	0.10128575	0.741	1.641	0.10128575	0.751	1.632	0.09620220	0.855
Cd ²⁺	1.535	0.05102457	0.811	1.541	0.05330850	0.819	1.531	0.04953859	0.995
Ca ²⁺	1.642	0.10185975	0.223	1.634	0.09731901	0.230	1.633	0.09675968	0.325
Sn ²⁺	1.777	0.19470705	0.275	1.778	0.19549490	0.286	1.765	0.18535099	0.338
Sr ²⁺	1.777	0.19470705	0.121	1.778	0.19549490	0.137	1.763	0.18380968	0.175
Ba ²⁺	1.936	0.33132862	0.062	1.937	0.33223312	0.072	1.924	0.32049456	0.096

Table 3. Simulated HFE, IOD, and CN Values for the Parameters Given in Table 2

	TIP3P			SPC/E			TIP4P _{EW}		
	HFE (kcal/mol)	IOD (Å)	CN	HFE (kcal/mol)	IOD (Å)	CN	HFE (kcal/mol)	IOD (Å)	CN
Be ²⁺	-572.8	1.64	4.4	-572.6	1.65	4.3	-572.4	1.64	4.0
Cu ²⁺	-479.8	2.11	6.2	-481.4	2.11	6.0	-480.0	2.11	6.1
Ni ²⁺	-473.1	2.06	6.0	-473.1	2.06	6.0	-472.7	2.06	6.0
Zn ²⁺	-467.0	2.09	6.0	-468.2	2.09	6.0	-467.4	2.09	6.0
Co ²⁺	-457.5	2.10	6.0	-456.8	2.10	6.0	-456.7	2.10	6.0
Cr ²⁺	-441.4	2.08	6.0	-442.0	2.08	6.0	-442.1	2.08	6.0
Fe ²⁺	-439.5	2.11	6.0	-439.8	2.11	6.0	-439.7	2.11	6.0
Mg ²⁺	-436.6	2.09	6.0	-436.7	2.09	6.0	-437.9	2.09	6.0
V ²⁺	-435.9	2.21	7.0	-435.5	2.21	6.8	-436.1	2.22	7.0
Mn ²⁺	-421.2	2.19	6.8	-420.3	2.20	6.5	-420.9	2.20	6.7
Hg ²⁺	-420.0	2.41	8.0	-420.6	2.41	8.0	-421.6	2.41	8.0
Cd ²⁺	-419.4	2.30	7.8	-419.4	2.30	7.5	-420.1	2.30	7.7
Ca ²⁺	-360.6	2.46	8.0	-360.6	2.46	8.0	-359.6	2.46	8.0
Sn ²⁺	-356.1	2.62	9.0	-356.1	2.62	8.8	-356.8	2.62	8.9
Sr ²⁺	-330.4	2.64	8.9	-330.3	2.64	8.7	-329.4	2.64	8.9
Ba ²⁺	-299.4	2.83	9.3	-298.6	2.83	9.2	-298.2	2.83	9.5
avg error	0.1	0.00	0.6	0.0	0.00	0.5	0.0	0.00	0.6
SD	0.5	0.01	0.9	0.6	0.01	0.9	0.5	0.01	0.9
unsigned avg error	0.4	0.00	0.6	0.4	0.00	0.5	0.4	0.00	0.6

used in the simulations. The Cl⁻ parameter employed in the simulations came from the work of Joung and Cheatham.⁶⁸

The IOD values of Mg²⁺ and Cl⁻ in the MgCl₂ systems are shown in Supporting Information Table SI.4. It can be seen that both the 12-6-4 parameter (which gives IOD ~2.11 Å) and the 12-6 CM set (which gives IOD ~2.08 Å) outperformed the original AMBER FF parameter (which gives IOD ~2.00 Å) with respect to the experimental value of 2.09 ± 0.04 Å.⁵⁴ For the Mg²⁺-nucleic acid system, Supporting Information Table SI.5 gives the IOD values as well as the Mg²⁺-backbone phosphate distance. We see that both the 12-6-4 parameter set and the 12-6 CM set have a remarkable improvement over the original Mg²⁺ parameter set in AMBER while the 12-6-4 model gives the best results.

Nonetheless, the 12-6-4 model may need further parameter refinement when employed with protein and nucleic acids systems since different fixed charge models are based on different parametrization philosophies. For example, the RESP

charge model used in AMBER FFs are based on gas-phase calculations at the HF/6-31G* level where the dipole moment overestimation is used to better approximate the liquid phase. This approximation may still cause some underestimation when compared to an experimental dipole moment (like the water models investigated in the present work). This situation needs to be further examined.

It is important to note that the HFE values of metal ions vary among different experimental analyses and the subsequent theoretical treatment of the experimental data. The present work relied on the approach of Marcus, in which he obtained the experimental HFE values of the metal ions based on the proton's HFE.⁵³ His analysis mostly used the conventional experimental values obtained from the National Bureau of Standards (NBS) compilation.⁶⁹ He used $\Delta_{\text{hyd}}G[H^+] = -1056 \pm 6$ kJ/mol, which is based on $\Delta_{\text{hyd}}H^0[H^+] = -1094$ kJ/mol, $\Delta_{\text{hyd}}S^0[H^+] = -131$ J/(K·mol), or $S_{\infty}[H^+(\text{aq})] = -22.2$ J/(K·mol).⁵³ However, there are different HFE values that have been

Table 4. Computed C_4 Values^a

	TIP3P	SPC/E	TIP4P _{EW}
Be ²⁺	186.5	188.1	228.5
Cu ²⁺	290.9	304.4	339.2
Ni ²⁺	212.8	205.2	259.2
Zn ²⁺	231.6	231.2	272.3
Co ²⁺	209.7	209.2	252.8
Cr ²⁺	136.8	131.2	177.4
Fe ²⁺	163.0	155.4	201.1
Mg ²⁺	132.9	122.2	180.5
V ²⁺	195.7	206.6	244.8
Mn ²⁺	146.1	154.9	192.3
Hg ²⁺	288.8	300.2	335.2
Cd ²⁺	185.6	198.8	233.7
Ca ²⁺	87.3	89.0	128.0
Sn ²⁺	187.9	201.1	231.4
Sr ²⁺	82.7	96.3	118.9
Ba ²⁺	71.9	85.8	112.5

^aÅ⁴·kcal/mol.

determined for the proton.^{70–74} Hence, there are different HFE values available for the metal ions studied herein.^{75,76} For example, Schmid et al. proposed a new set of HFE values for several monovalent and divalent ions⁷⁵ while Asthagiri et al. calculated the HFEs for the first transition row metals using a quasi-chemical theory of solutions.⁷⁶ The data in the SI from our scans of parameter space will be helpful for people who prefer to derive parameters utilizing different HFE values.

CONCLUSIONS

We showed earlier that the electrostatic plus 12–6 LJ potential nonbonded model underestimates the interactions between metal ions and the surrounding water molecules in PME simulations.³⁴ Via a consideration of the physical origin effect, we hypothesized that the charge–induced dipole interaction is responsible for the majority of this underestimation. In light of this, we proposed and parametrized a 12–6–4 LJ-type nonbonded model for M(II) ions in order to take into account the charge–induced dipole interaction. First we investigated the available parameter space via a series of scans of parameter space. Subsequently, we employed a fitting procedure, which treated the experimental HFE and IOD values as the target values. Unlike our former nonbonded model, the new nonbonded model reproduces the experimental HFE, IOD, and CN values simultaneously. Initial tests showed good performance when modeling aqueous MgCl₂ systems and Mg²⁺–nucleic acid systems. Further parametrization efforts may further increase the performance of the current model.

Generally, the 12–6–4 LJ-type nonbonded model provides a significant improvement over the former 12–6 LJ nonbonded model. It reproduces several different kinds of experimental data at the same time, which eliminates the need to develop compromise parameters as was done for the former nonbonded model in PME simulations. It is easy to incorporate the present model into typical biomolecular force fields with minimal additional computational cost. One caveat is that the new model does not consider the charge-transfer effect explicitly in the potential form, which may influence its ability to simulate systems with strong charge-transfer effects. Hence, care should be taken for systems like Be²⁺ and Hg²⁺ in aqueous solution due to the existence of strong charge-transfer effects.^{64,67}

ASSOCIATED CONTENT

Supporting Information

Details of the parameter fitting procedures, simulated HFE, IOD, and CN values for the parameters space scanning, and fitting curves for various metal ions in SPC/E and TIP4P_{EW} water models. Polarizability parameters, simulation procedures, and results for the aqueous MgCl₂ systems and Mg²⁺–nucleic acid systems. Uncertainty analyses of the HFE values. This material is available free of charge via the Internet at <http://pubs.acs.org>.

AUTHOR INFORMATION

Corresponding Author

*E-mail: kmerzl@gmail.com.

Notes

The authors declare no competing financial interest.

ACKNOWLEDGMENTS

We thank Dr. Sam Trickey (UF), Dr. Michael N. Weaver (UF), Dr. Dhruva K. Chakravorty (UF), Yipu Miao (UF), and Shuai Wang (UF) for many helpful discussions. We thank Dr. David Case (Rutgers) and Dr. Jason Swails (Rutgers) for help with programming within AMBER. We gratefully acknowledge financial support from the United States National Institutes of Health (RO1's GM044974 and GM066859) and computing support from the University of Florida High Performance Computing Center.

ABBREVIATIONS

HFE, hydration free energy; CN, coordination number; PME, particle mesh ewald; RDF, radial distribution function; LJ, Lennard-Jones; TI, thermodynamic integration; VDW, van der Waals; IOD, ion–oxygen distance

REFERENCES

- (1) Tus, A.; Rakipović, A.; Peretin, G.; Tomić, S.; Šikić, M. *Nucleic Acids Res.* **2012**, *40*, W352–W357.
- (2) Waldron, K. J.; Robinson, N. J. *Nat. Rev. Microbiol.* **2009**, *7*, 25–35.
- (3) Rosenzweig, A. C. *Chem. Biol.* **2002**, *9*, 673–677.
- (4) Thomson, A. J.; Gray, H. B. *Curr. Opin. Chem. Biol.* **1998**, *2*, 155–158.
- (5) Dupureur, C. M. *Curr. Opin. Chem. Biol.* **2008**, *12*, 250–255.
- (6) Andreini, C.; Bertini, I.; Cavallaro, G.; Holliday, G.; Thornton, J. *J. Biol. Inorg. Chem.* **2008**, *13*, 1205–1218.
- (7) Chaturvedi, U. C.; Shrivastava, R. *FEMS Immunol. Med. Microbiol.* **2005**, *43*, 105–114.
- (8) Berridge, M. J.; Bootman, M. D.; Lipp, P. *Nature* **1998**, *395*, 645–648.
- (9) Christianson, D. W. *Prog. Biophys. Mol. Biol.* **1997**, *67*, 217–252.
- (10) Lipscomb, W. N.; Sträter, N. *Chem. Rev.* **1996**, *96*, 2375–2434.
- (11) Linder, M. C.; Hazegh-Azam, M. *Am. J. Clin. Nutr.* **1996**, *63*, 797S–811S.
- (12) Holm, R. H.; Kennepohl, P.; Solomon, E. I. *Chem. Rev.* **1996**, *96*, 2239–2314.
- (13) Coleman, J. E. *Annu. Rev. Biochem.* **1992**, *61*, 897–946.
- (14) Berg, J. M. *Annu. Rev. Biophys. Biophys. Chem.* **1990**, *19*, 405–421.
- (15) Toukmaji, A.; Sagui, C.; Board, J.; Darden, T. *J. Chem. Phys.* **2000**, *113*, 10913–10927.
- (16) Petersen, H. G. *J. Chem. Phys.* **1995**, *103*, 3668.
- (17) Cheatham, T. E., III; Miller, J. L.; Fox, T.; Darden, T. A.; Kollman, P. A. *J. Am. Chem. Soc.* **1995**, *117*, 4193–4194.
- (18) Darden, T.; York, D.; Pedersen, L. *J. Chem. Phys.* **1993**, *98*, 10089–10092.

- (19) Gresh, N.; Claverie, P.; Pullman, A. *Theor. Chim. Acta* **1984**, *66*, 1–20.
- (20) Tiraboschi, G.; Roques, B. P.; Gresh, N. *J. Comput. Chem.* **1999**, *20*, 1379–1390.
- (21) Tiraboschi, G.; Gresh, N.; Giessner-Prettre, C.; Pedersen, L. G.; Deerfield, D. W. *J. Comput. Chem.* **2000**, *21*, 1011–1039.
- (22) de Courcy, B.; Piquemal, J.-P.; Gresh, N. *J. Chem. Theory Comput.* **2008**, *4*, 1659–1668.
- (23) Gresh, N.; de Courcy, B.; Piquemal, J.-P.; Foret, J.; Courtiol-Legourd, S.; Salmon, L. *J. Phys. Chem. B* **2011**, *115*, 8304–8316.
- (24) Stote, R. H.; Karplus, M. *Proteins: Struct., Funct., Bioinf.* **1995**, *23*, 12–31.
- (25) Pang, Y.-P. *Proteins: Struct., Funct., Bioinf.* **2001**, *45*, 183–189.
- (26) Chillemi, G.; D'Angelo, P.; Pavel, N. V.; Sanna, N.; Barone, V. *J. Am. Chem. Soc.* **2002**, *124*, 1968–1976.
- (27) Sakharov, D. V.; Lim, C. *J. Am. Chem. Soc.* **2005**, *127*, 4921–4929.
- (28) Sakharov, D. V.; Lim, C. *J. Comput. Chem.* **2009**, *30*, 191–202.
- (29) Peters, M. B.; Yang, Y.; Wang, B.; Füsti-Molnár, L. s.; Weaver, M. N.; Merz, K. M. *J. Chem. Theory Comput.* **2010**, *6*, 2935–2947.
- (30) Wu, J. C.; Piquemal, J.-P.; Chaudret, R.; Reinhardt, P.; Ren, P. *J. Chem. Theory Comput.* **2010**, *6*, 2059–2070.
- (31) Wu, R.; Lu, Z.; Cao, Z.; Zhang, Y. *J. Chem. Theory Comput.* **2011**, *7*, 433–443.
- (32) Zhang, J.; Yang, W.; Piquemal, J.-P.; Ren, P. *J. Chem. Theory Comput.* **2012**, *8*, 1314–1324.
- (33) Zhu, T.; Xiao, X.; Ji, C.; Zhang, J. Z. *J. Chem. Theory Comput.* **2013**, *9*, 1788–1798.
- (34) Li, P.; Roberts, B. P.; Chakravorty, D. K.; Merz, K. M. *J. Chem. Theory Comput.* **2013**, *9*, 2733–2748.
- (35) Cornell, W. D.; Cieplak, P.; Bayly, C. I.; Gould, I. R.; Merz, K. M.; Ferguson, D. M.; Spellmeyer, D. C.; Fox, T.; Caldwell, J. W.; Kollman, P. A. *J. Am. Chem. Soc.* **1995**, *117*, 5179–5197.
- (36) MacKerell, A. D.; Bashford, D.; Bellott, M.; Dunbrack, R.; Evanseck, J.; Field, M. J.; Fischer, S.; Gao, J.; Guo, H.; Ha, S. a. *J. Phys. Chem. B* **1998**, *102*, 3586–3616.
- (37) Jorgensen, W. L.; Maxwell, D. S.; Tirado-Rives, J. *J. Am. Chem. Soc.* **1996**, *118*, 11225–11236.
- (38) Jorgensen, W. L.; Chandrasekhar, J.; Madura, J. D.; Impey, R. W.; Klein, M. L. *J. Chem. Phys.* **1983**, *79*, 926–935.
- (39) Berendsen, H. J. C.; Grigera, J. R.; Straatsma, T. P. *J. Phys. Chem.* **1987**, *91*, 6269–6271.
- (40) Horn, H. W.; Swope, W. C.; Pitera, J. W.; Madura, J. D.; Dick, T. J.; Hura, G. L.; Head-Gordon, T. *J. Chem. Phys.* **2004**, *120*, 9665–9678.
- (41) Mezei, M. *J. Chem. Phys.* **1987**, *86*, 7084–7088.
- (42) Straatsma, T. P.; Berendsen, H. J. C. *J. Chem. Phys.* **1988**, *89*, 5876–5886.
- (43) Mitchell, M. J.; McCammon, J. A. *J. Comput. Chem.* **1991**, *12*, 271–275.
- (44) Kollman, P. *Chem. Rev.* **1993**, *93*, 2395–2417.
- (45) Beutler, T. C.; Mark, A. E.; van Schaik, R. C.; Gerber, P. R.; van Gunsteren, W. F. *Chem. Phys. Lett.* **1994**, *222*, 529–539.
- (46) Hummer, G.; Szabo, A. *J. Chem. Phys.* **1996**, *105*, 2004–2010.
- (47) Simonson, T.; Carlsson, J.; Case, D. A. *J. Am. Chem. Soc.* **2004**, *126*, 4167–4180.
- (48) Steinbrecher, T.; Mobley, D. L.; Case, D. A. *J. Chem. Phys.* **2007**, *127*, 214108–214113.
- (49) Shirts, M. R.; Pitera, J. W.; Swope, W. C.; Pande, V. S. *J. Chem. Phys.* **2003**, *119*, 5740–5761.
- (50) Ryckaert, J.-P.; Ciccotti, G.; Berendsen, H. J. *J. Comput. Phys.* **1977**, *23*, 327–341.
- (51) Miyamoto, S.; Kollman, P. A. *J. Comput. Chem.* **1992**, *13*, 952–962.
- (52) Bayly, C. I.; Cieplak, P.; Cornell, W.; Kollman, P. A. *J. Phys. Chem.* **1993**, *97*, 10269–10280.
- (53) Marcus, Y. *J. Chem. Soc., Faraday Trans.* **1991**, *87*, 2995–2999.
- (54) Marcus, Y. *Chem. Rev.* **1988**, *88*, 1475–1498.
- (55) Miyanaga, T.; Watanabe, I.; Ikeda, S. *Chem. Lett.* **1988**, *17*, 1073–1076.
- (56) Ohtaki, H.; Radnai, T. *Chem. Rev.* **1993**, *93*, 1157–1204.
- (57) Jalilehvand, F.; Spångberg, D.; Lindqvist-Reis, P.; Hermansson, K.; Persson, I.; Sandström, M. *J. Am. Chem. Soc.* **2000**, *123*, 431–441.
- (58) Smirnov, P. R.; Trostin, V. N. *Russ. J. Gen. Chem.* **2011**, *81*, 282–289.
- (59) Eisenberg, D. S.; Kauzmann, W. *The Structure and Properties of Water*; Oxford University Press, 1969.
- (60) Dyke, T. R.; Muentner, J. S. *J. Chem. Phys.* **1973**, *59*, 3125–3127.
- (61) Gubskaya, A. V.; Kusalik, P. G. *J. Chem. Phys.* **2002**, *117*, 5290–5302.
- (62) Silvestrelli, P. L.; Parrinello, M. *J. Chem. Phys.* **1999**, *111*, 3572–3580.
- (63) Ren, P.; Ponder, J. W. *J. Phys. Chem. B* **2003**, *107*, 5933–5947.
- (64) Pavlov, M.; Siegbahn, P. E.; Sandström, M. *J. Phys. Chem. A* **1998**, *102*, 219–228.
- (65) Irving, H.; Williams, R. *J. Chem. Soc.* **1953**, 3192–3210.
- (66) Gorelsky, S. I.; Basumallick, L.; Vura-Weis, J.; Sarangi, R.; Hodgson, K. O.; Hedman, B.; Fujisawa, K.; Solomon, E. I. *Inorg. Chem.* **2005**, *44*, 4947–4960.
- (67) Tai, H.-C.; Lim, C. *J. Phys. Chem. A* **2006**, *110*, 452–462.
- (68) Joung, I. S.; Cheatham, T. E. *J. Phys. Chem. B* **2008**, *112*, 9020–9041.
- (69) Wagman, D. D.; Evans, W. H.; Parker, V. B.; Schumm, R. H.; Halow, I. *The NBS tables of chemical thermodynamic properties. Selected values for inorganic and C1 and C2 organic substances in SI units*, DTIC Document, 1982.
- (70) Tawa, G. J.; Topol, I. A.; Burt, S. K.; Caldwell, R. A.; Rashin, A. A. *J. Chem. Phys.* **1998**, *109*, 4852–4863.
- (71) Tissandier, M. D.; Cowen, K. A.; Feng, W. Y.; Gundlach, E.; Cohen, M. H.; Earhart, A. D.; Coe, J. V.; Tuttle, T. R. *J. Phys. Chem. A* **1998**, *102*, 7787–7794.
- (72) Topol, I. A.; Tawa, G. J.; Burt, S. K.; Rashin, A. A. *J. Chem. Phys.* **1999**, *111*, 10998–11014.
- (73) Mejias, J. A.; Lago, S. *J. Chem. Phys.* **2000**, *113*, 7306–7316.
- (74) Zhan, C.-G.; Dixon, D. A. *J. Phys. Chem. A* **2001**, *105*, 11534–11540.
- (75) Schmid, R.; Miah, A. M.; Sapunov, V. N. *Phys. Chem. Chem. Phys.* **2000**, *2*, 97–102.
- (76) Asthagiri, D.; Pratt, L. R.; Paulaitis, M. E.; Rempe, S. B. *J. Am. Chem. Soc.* **2004**, *126*, 1285–1289.

■ NOTE ADDED AFTER ASAP PUBLICATION

This article was posted ASAP on November 21, 2013. Additional information has been added to the Supporting Information. The correct version was published on November 25, 2013.